41st AIAA Thermophysics Conference
22 - 25 June 2009, San Antonio, Texas

AIAA 2009-3597

Strongly coupled computation of material response and nonequilibrium flow for hypersonic ablation

Alexandre Martin* and Iain D. Boyd†

Department of Aerospace Engineering, The University of Michigan, Ann Arbor, MI, 48109, USA

A one-dimensional material response implicit solver with surface ablation and pyrolysis is strongly coupled to LeMANS, a CFD code for the simulation of weakly ionized hypersonic flows in thermo-chemical non-equilibrium. Using blowing wall boundary conditions and a moving mesh algorithm, the results of a strongly coupled solution of a re-entry problem are presented, using the well defined case of the IRV-2 vehicle. Results are compared to other coupled codes and show good agreement with published numerical results.

Nomenclature

Symbols

$\mathbf{A}$	Jacobian matrix	$\mathbf{R}$	Right hand side term
a	Speed of sound	$\mathbf{r}$	Distance vector
$\mathbf{d}$	Mesh edge length	$\mathbf{S}, S$	Surface
$\mathbf{C}$	Source term vector	t	Time
$\mathbf{e}, E$	Energy	T	Temperature
$\mathbf{F}$	Inviscid flux vector	T_v	Vibrational temperature
$\mathbf{F_d}$	Diffusive flux vector	$\mathbf{U}$	Conservative vector
$\mathbf{F_n}$	Normal total flux vector	$\mathbf{u}, u, v$	Velocity
Fo	Forchheimer number	$\mathbf{w}, w$	Source term, Node velocity
$\mathbf{G}$	Partial flux vector, $\mathbf{G} = \mathbf{F} - \mathbf{F_d} - \mathbf{uU}$	$\bar{w}_n$	Mean normal face velocity
h	Enthalpy	v'	Superficial velocity; $v' = \phi v$
$\mathbf{I}$	Identity matrix	V	Volume
$\mathbf{J}$	Directional species diffusion flux tensor	x, y	Coordinates
k	Spring coefficient	Y_i	Species mass fraction
K	Permeability	β	Forchheimer coefficient
l	Characteristic length	$\boldsymbol{\delta}$	Length edge variation
l_s	Characteristic length of the volume increment	$\mathbf{\Lambda}$	Eigenvalue matrix
$\mathbf{L}$	Eigenvector similarity transformation matrix	μ	Dynamic viscosity
$\dot{m}'''$	Volumetric mass source term	ρ	Density
$\dot{m}$	Mass flux	$\boldsymbol{\tau}$	Viscous tensor
p	Pressure	ϕ	Porosity
p_η	Conserved pressure in the normal direction	ψ	implicit-time relaxation damping factor
$\dot{q}''$	Internal heat flux		
$\mathbf{q}$	Surface heat transfer rate		

Subscripts and Superscripts

*Research Fellow, AIAA Member.
†Professor, Associate Fellow AIAA.

0	Non blowing	r	Rotational
c	Char	s	Solid
cv	Control volume	$\mathbf{T}$	Transposed
cs	Control surface	v	Virgin, Vibrational
e	Electron and electronic excitation	w	Wall
f	Fixed mesh	x, y, z	Coordinates
g	Gas	∞	Freestream

I. Introduction

The Thermal Protection System (TPS) of a re-entry vehicle is one of the key components of its design. The material used for the TPS can be classified into two main categories: ablative materials, as in the one used on Apollo missions, and non-ablative materials, such as the ceramic tiles used on the space shuttle. The theory behind the use of ablators is quite simple; the energy absorbed by the removal of material from the surface is not used to heat the TPS, thus keeping the vehicle at a reasonably "cold" temperature. In order to properly model the heat rate at the surface of the vehicle, the ablating boundary condition must take into account many phenomena: surface recession, wall temperature, blowing rates, gas composition, surface chemistry, etc. One way to account for effects of the TPS on the surface flow is to link a material response model to the flow solver.[1–4]

In order to do this, modifications to the flow solver were made,[5,6] especially at the wall, where ablating gases need to be introduced in the flow field. To dynamically account for the effects of the surface recession on the flow field, the mesh of the flow field simulation has been allowed to move as the surface ablates. This methodology allows calculation of the discrete points in a re-entry trajectory, and therefore allows prediction of recession rates and wall temperature. These two parameters are essential to heat shield design, and therefore mission design.

First, the flow solver and material response solver used to perform the coupling are presented. Next, the necessary modifications to the flow solver are presented, as well as the coupling strategies. Finally, in order to demonstrate the coupling method, the simulation of the re-entry of the generic IRV-2 vehicle is presented.

II. LeMANS: an unstructured tridimensional Navier-Stokes solver for hypersonic nonequilibrium aerothermodynamics

II.A. Overview

LeMANS is a finite volume Navier-Stokes solver currently being developed at The University of Michigan.[7–10] The code assumes that the rotational and translational energy modes of all species can be described by their respective temperatures T_r and T, and that the vibrational energy mode of all species and the electronic energy can be described by a single temperature T_{ve}.[11] The latter is computed using the species vibrational energy, modeled as a harmonic oscillator. The viscous stresses are modeled assuming a Newtonian fluid, using Stokes' hypothesis, and the species mass diffusion fluxes are modeled using a modified version of Fick's law. Mixture transport properties are calculated using one of two models; the first uses Wilke's semi-empirical mixing rule with species viscosities calculated using Blottner's model and species thermal conductivities determined using Eucken's relation, and the other uses Gupta's mixing rule with species viscosities and thermal conductivities calculated using non-coulombic/coulombic collision cross section data. Heat fluxes are modeled according to Fourier's law for all temperatures. Finally, the source terms of the species conservation equations are modeled using a standard finite-rate chemistry model for reacting air in conjunction with Park's two-temperature model to account for thermal nonequilibrium effects on the reaction rates.

Numerically, the code has the capability to handle any mix of hexahedra, tetrahedra, prisms and pyramids meshes in 3D or triangles and quadrilaterals in 2D. Numerical fluxes between the cells are discretized using a modified Steger-Warming Flux Vector Splitting which has low dissipation and is appropriate to calculate boundary layers. A point or line implicit method is used to perform the time integration. The code has been extensively validated against experimental data, and has also been compared to other similar codes such as NASA Ames' DPLR[12] and NASA Langley's LAURA.[13]

II.B. Governing equations

With the approximations mentioned above, the conservation equations for a three-dimensional system can be written as

$$\frac{\partial \mathbf{U}}{\partial t} + \nabla \cdot (\mathbf{F} - \mathbf{F_d}) = \mathbf{C} \tag{1}$$

where

$$\mathbf{U} = \begin{pmatrix} \rho_1 \\ \vdots \\ \rho_{ns} \\ \rho u_x \\ \rho u_y \\ \rho u_z \\ E \\ E_{ve} \\ E_r \end{pmatrix} \quad \text{and} \quad \mathbf{C} = \begin{pmatrix} \dot{w}_1 \\ \vdots \\ \dot{w}_{ns} \\ 0 \\ 0 \\ 0 \\ 0 \\ \dot{w}_v \\ \dot{w}_r \end{pmatrix}$$

are the vector of conserved variables and the vector of source terms, respectively. In these expressions, $\rho_1 \dots \rho_{ns}$ are the species densities, u_i are the bulk velocity components, E, E_{ve} and E_r are the total, the vibrational-electronic and the rotational energy per unit volume of mixture, respectively.

The inviscid and diffusive flux matrices are given by

$$\mathbf{F} = \begin{pmatrix} \rho_1 u_x & \rho_1 u_y & \rho_1 u_z \\ \vdots & \vdots & \vdots \\ \rho_{ns} u_x & \rho_{ns} u_x & \rho_{ns} u_x \\ \rho u_x^2 + p & \rho u_y u_x & \rho u_z u_x \\ \rho u_x u_y & \rho u_y^2 + p & \rho u_z u_y \\ \rho u_x u_z & \rho u_y u_z & \rho u_z^2 + p \\ (E+p) u_x & (E+p) u_y & (E+p) u_z \\ E_{ve} u_x & E_{ve} u_y & E_{ve} u_z \\ E_r u_x & E_r u_y & E_r u_z \end{pmatrix}$$

and

$$\mathbf{F_d} = \begin{pmatrix} -J_{x,1} & -J_{y,1} & -J_{z,1} \\ \vdots & \vdots & \vdots \\ -J_{x,ns} & -J_{y,ns} & -J_{z,ns} \\ \tau_{xx} & \tau_{xy} & \tau_{xz} \\ \tau_{yx} & \tau_{yy} & \tau_{yz} \\ \tau_{zx} & \tau_{zy} & \tau_{zz} \\ \multicolumn{3}{c}{\mathbf{u\tau} - (\mathbf{q}_t + \mathbf{q}_r + \mathbf{q}_{ve}) - (\mathbf{h^T J})} \\ \multicolumn{3}{c}{-\mathbf{q}_{ve} - (\mathbf{e}_{ve}^{\mathbf{T}} \mathbf{J})} \\ \multicolumn{3}{c}{-\mathbf{q}_r - (\mathbf{e}_r^{\mathbf{T}} \mathbf{J})} \end{pmatrix}$$

where p is the pressure, τ_{ij} is the viscous tensor components and $\mathbf{q}_t$, $\mathbf{q}_r$ and $\mathbf{q}_{ve}$ are respectively the directional translational, rotational and vibrational-electronic heat fluxes vector. Moreover, $\mathbf{h}$ is the species enthalpy vector and $\mathbf{J}$ is the directional species diffusion flux tensor. More details on these equations and on the modeling of the individual terms can be found in Ref. 8.

Equation 1 can be reduced to a simple vector form which splits the flux tensor using the conservative

vector:

$$\frac{\partial}{\partial t}\begin{pmatrix}\boldsymbol{\rho}\\ \rho\mathbf{u^T}\\ E\\ E_{ve}\\ E_r\end{pmatrix}+\nabla\cdot\left[\begin{pmatrix}\boldsymbol{\rho}\\ \rho\mathbf{u^T}\\ E\\ E_{ve}\\ E_r\end{pmatrix}\mathbf{u}+\begin{pmatrix}0\\ \mathbf{I}p\\ \mathbf{u}p\\ 0\\ 0\end{pmatrix}-\begin{pmatrix}-\mathbf{J}\\ \boldsymbol{\tau}\\ \mathbf{u}\boldsymbol{\tau}-(\mathbf{q}_t+\mathbf{q}_r+\mathbf{q}_{ve})-(\mathbf{h^T J})\\ -\mathbf{q}_{ve}-(\mathbf{e}_{ve}^{\mathbf{T}}\mathbf{J})\\ -\mathbf{q}_r-(\mathbf{e}_r^{\mathbf{T}}\mathbf{J})\end{pmatrix}\right]=\begin{pmatrix}\dot{\mathbf{w}}\\ 0\\ 0\\ \dot{w}_v\\ \dot{w}_r\end{pmatrix}$$

which can be re-reduced to:

$$\frac{\partial \mathbf{U}}{\partial t}+\nabla\cdot(\mathbf{U}\mathbf{u}+\mathbf{G})=\mathbf{C} \tag{2}$$

III. MOPAR: a material response code

The material response code used in this validation is currently being developed at The University of Michigan, and is called MOPAR (Modeling of Pyrolysis and Ablation Response).[14] The code employs the same methodology as the one created at North Carolina State University and Sandia National Laboratories,[15–18] and uses the Control Volume Finite-Element Method (CVFEM) to model surface ablation with wall recession, as well as inner decomposition and pyrolysis gas behavior. The model is described by the following four governing equations:

Mixture Energy Equation

$$\frac{d}{dt}\int_{cv}\rho E dV-\int_{cs}\rho h v_{cs}dS+\int_{cs}\phi\rho_g h_g v_g dS\ \ +\int_{cs}\dot{q}''dA=0 \tag{3}$$

Solid Phase Equation

$$\frac{d}{dt}\int_{cv}\rho_s dV-\int_{cs}\rho_s v_{cs}dS-\int_{cv}\dot{m}_s'''dV=0 \tag{4}$$

Gas Phase Continuity Equation

$$\frac{d}{dt}\int_{cv}\phi\rho_g dV-\int_{cs}\phi\rho_g v_{cs}dS+\int_{cs}\phi\rho_g v_g dS-\int_{cv}\dot{m}_g'''dV=0 \tag{5}$$

Momentum Equation: Forchheimer's Law

$$\frac{\partial P}{\partial x}=-\frac{\mu}{K}v_g'(1+\mathrm{Fo}) \tag{6}$$

The first terms in Eqs. 3 to 5 account, respectively, for the energy, solid mass, and gas mass content, and the second terms account for the grid convection. The third terms in Eqs. 3 and 5 represent the gas mass flux, and the last terms in Eqs. 4 to 5, the sources. The last term of Eq. 3 accounts for the heat conduction within the solid. In Eq. 6, Forchheimer's Law, the Forchheimer Number (Fo), is given by

$$\mathrm{Fo}=\frac{\beta K\rho v_g'}{\mu}$$

This number indicates when microscopic effects (pore size) are perceivable at a macroscopic (geometry size) level. In this formulation, if $\mathrm{Fo}\ll 1$, the term in parenthesis in Eq. 6 can be approximated as 1, and the equation simply reduces to Darcy's law. Therefore, it is more logical to use the Forchheimer Number to predict non-Darcian flow, and thus more rigorous to use Forchheimer's law.

The first two of these four equations are solved implicitly on an arbitrary contracting grid using Landau coordinates. Newton's method for non-linear systems is used to solve both equations sequentially. The third equation is straightforward, and can be solved analytically. Forchheimer's law is explicitly solved for v_g and directly integrated in the gas-phase continuity equation.

In addition to the improvement in the momentum equation,[5] the present code also takes into account variable coordinate systems (cylindrical and spherical), and allows ablation on both sides of the domain, using a new tri-diagonal solver.[19] The code is validated against experimental data and code-to-code comparisons, as discussed in Ref. 14.

IV. Modifications to the flow solver

IV.A. Blowing boundary conditions

To account for the coupling between the flow field and the material response, ablation is added to the CFD code; therefore, a modification to the surface boundary condition is necessary. In order to implement the blowing boundary condition, the first cell near the blowing wall is used as a control volume.[20] The physical values that need to be imposed at the wall are the temperature T_w, the blowing mass flow rate $\dot{m}_w = \rho_w v_w$ and the species mass fraction Y_{wi}. Conservation of momentum is enforced at the wall, using the neighboring cell (subscript nc) and assuming that the ablation gas flow is perpendicular to the surface:

$$p_\eta = p_{nc} + \rho_{nc} v_{nc}^2 = p_w(\rho_w, T_w) + \rho_w v_w^2$$

Using the perfect gas relation at the wall, this equation can be rearranged to obtain the primitive variables:

$$\rho_w = \frac{p_\eta + \sqrt{p_\eta^2 - 4RT_w \dot{m}_w^2)}}{2RT_w}$$

$$v_w = \frac{2RT_w \dot{m}_w}{p_\eta + \sqrt{p_\eta^2 - 4RT_w \dot{m}_w^2)}}$$

$$p_w = \frac{p_\eta + \sqrt{p_\eta^2 - 4RT_w \dot{m}_w^2)}}{2}$$

Once values are computed for the primitive variables, the conservative quantities in the ghost cells of the boundary are set such that the flux across the wall is the required blowing flux. This blowing boundary condition has been tested over a wide range of blowing rates, assuring the robustness of the implementation. Following the methodology for the verification and validations of NASA Ames' DPLR code[21] and NASA Langley's LAURA code,[20] the blowing boundary of LeMANS has also been verified and validated.[5,6]

IV.B. Moving mesh

In order to complete the strong coupling of the thermal response code MOPAR to the hypersonic CFD code LeMANS, moving mesh capabilities are added to the latter code. The method chosen has been proposed by Ref. 22; the Geometric Conservation Law, is solved implicitly in the discretized governing equations. This method has the advantage of being valid for both explicit and implicit schemes, works on any kind of mesh cells, is easy to implement in a finite volume scheme developed for fixed meshes, and retains the order of accuracy of the scheme.

To implement the method, the flow solver must be modified when performing the computation of the fluxes, as well as during time integration.

IGCL formulation

Integrated over an arbitrary volume, Eq. 2 can be written for an arbitrarily moving system (Arbitrary Lagragian-Eulerian formulation):

$$\frac{\partial}{\partial t}\int_{cv} \mathbf{U} dV + \oint_{cs} (\mathbf{Uu} - \mathbf{Uw} + \mathbf{G}) \cdot \mathbf{dS} = \int_{cv} \mathbf{C} dV \tag{7}$$

where $\mathbf{S}$ is a vector area element of surface cs, which is one of the enclosing surfaces of the time-dependent volume cv; $\mathbf{u}$ is the velocity of the fluid; and $\mathbf{w}$ is the arbitrarily specified velocity of cs.

According to Ref. 22, the discretization of the governing equation for a finite volume scheme is

$$V^{t+1}\mathbf{U}^{t+1} - V^t \mathbf{U}^t = -\sum_k \mathbf{F}_{\mathbf{n},k} S_k \Delta t + V \mathbf{C} \Delta t \tag{8}$$

where $\mathbf{F_n} = \mathbf{F}\mathbf{n}^\mathbf{T}$ and $\mathbf{n} = (n_x\ n_y\ n_z)$ is the normal vector of the face S. When applied to Eq. 2, we obtain:

$$\mathbf{F_n} = \mathbf{U}(u_n - \bar{w}_n) + \mathbf{G}\mathbf{n}^\mathbf{T}$$

where

$$\bar{w}_n = \frac{\Delta V}{S\Delta t}$$

and where ΔV is the face volumetric increment calculated according to the type of elements. These quantities are calculated in such a way that the volumetric increment is balanced by the flux generated by the face movement, so that in the end, the conserved quantity remains unchanged by the moving mesh. For a planar 2D geometry, the volume increment is

$$\Delta V = \Delta t \ \mathbf{w_0} \times \Delta \mathbf{r}_{\mathbf{12}}^{n+1/2}$$

where $\mathbf{w_0}$ is the average velocity of the two nodes of the side, and $\mathbf{r}_{\mathbf{12}}^{n+1/2}$ is the time averaged side vector. For axi-symmetric geometry, the volume becomes

$$\Delta V = \frac{\Delta t}{6}(2y_1^{n+1/2} + y_2^{n+1/2})\mathbf{w_1} \times \Delta \mathbf{r}_{\mathbf{12}}^n + \frac{\Delta t}{6}(2y_2^{n+1/2} + y_1^{n+1/2})\mathbf{w_2} \times \Delta \mathbf{r}_{\mathbf{12}}^n + \frac{\Delta t^2}{4}(y_1^{n+2/3} + y_2^{n+2/3})\mathbf{w_1} \times \mathbf{w_2}$$

For 3D tetrahedron volumes, the expression is

$$\Delta V = \Delta t \ \mathbf{w_0} \cdot \mathbf{S}^{n+1/2} + \frac{\Delta t^3}{24}\mathbf{w_1} \cdot \mathbf{w_2} \times \mathbf{w_3}$$

where $\mathbf{w_0}$ is now the average velocity of the three nodes of the side, and $\mathbf{S} = \frac{1}{2}\Delta \mathbf{r_{12}} \times \Delta \mathbf{r_{13}}$. This expression takes into account the fact that in 3D, the order in which the nodes are moved leads to different facial volumes. This expression is therefore an average of all the possible movement combinations. It is to be noted that this last equation can be used for any 3D volumetric cells by dividing them into multiple tetrahedrons.

Flux splitting

The Jacobian matrix needed to compute the Steger-Warming Flux Splitting Scheme used by the inviscid part of the governing equations is :

$$\mathbf{A} = \mathbf{A}^f - \mathbf{I}\bar{w}_n$$

where superscript f refers to the value calculated for a fixed mesh. The eigenvalue matrix of $\mathbf{A}$ is therefore:

$$\mathbf{\Lambda} = \mathbf{\Lambda}^f - \mathbf{I}\bar{w}_n$$

As for the similarity transformation matrix $\mathbf{L}$, constructed from the eigenvectors, it is identical to the one calculated for a fixed mesh.

$$\mathbf{L} = \mathbf{L}^f$$

This development shows that in order to add moving grid capability to the Flux Splitting Scheme of LeMANS, only the eigenvalues need to be modified.

Implicit time integration

For the types of hypersonic problems solved using LeMANS, an implicit time integration is necessary to take advantage of the larger allowable time steps. Using a Taylor expansion on Eq. 8, the implicit time integration becomes

$$\mathbf{R}^{t+1} = \mathbf{R}^t + \left[\frac{\partial \mathbf{R}}{\partial \mathbf{U}}\right]^t \left(\mathbf{U}^{t+1} - \mathbf{U}^t\right) + \left[\frac{\partial \mathbf{R}}{\partial V}\right]^t \left(V^{t+1} - V^t\right)$$

where $-\mathbf{R}$ is the right-hand-side of Eq. 8. After some manipulation, the time integration becomes

$$\mathbf{U}^{t+1} = \mathbf{U}^t + \left[\frac{V^t + \Delta V}{\Delta t}\mathbf{I} + \left[\frac{\partial \mathbf{R}}{\partial \mathbf{U}}\right]^t\right]^{-1} \left(-\mathbf{R}^t - \left[\frac{\partial \mathbf{R}}{\partial V}\right]^t \Delta V - \mathbf{U}^t \frac{\Delta V}{\Delta t}\right)$$

It is to be noted that in order to balance the flux, it is necessary to evaluate the source term using the volumetric time increment: this translates to:

$$\mathbf{R}^t = \sum_k \mathbf{F}_{\mathbf{n},k}^t S_k^t - (V^t + \Delta V)\mathbf{C}$$

Mesh movement description

Even though the mathematics of the moving mesh is fairly simple, the question of how the mesh moves needs to be defined. In the context of ablation, because only the wall moves, the rest of the mesh can simply follow proportionally. In order to do so, a spring analogy is applied to each edge i of the mesh, and the system is solved for the static equilibrium:[23]

$$\sum \mathbf{F}_i = -\sum k_i \boldsymbol{\delta}_i = 0$$

where $\boldsymbol{\delta}_i$ is the variation of the length of edge i caused by the mesh movement. In order to preserve the proportionality of the mesh, the spring coefficient is inversely proportional to the edge length ($\mathbf{d}$) prior to the movement:

$$k_i = \frac{1}{|\mathbf{d}_i|}$$

With this approach, it is impossible to generate negative volumes, and the proportionality makes sure that the mesh can still capture the boundary layer and the shock relatively well. Numerically, however, the cost is higher than other methods, like, for instance, applying Landau transformation coordinates to the flow field. Since the static equilibrium is calculated at each node, the equation requires to invert a $n \times n$ matrix for each dimension, where n is the number of nodes. However, since the matrix is symmetric, it can be solved with relative ease using a pre-conditioned conjugate gradient method (or one of the Krylov subspace methods, for that matter).

This approach still poses problems when dealing with domain decomposition for multi-processor computing. Because, as opposed to cells, nodes are shared by processors, and they absolutely need to move identically on each sub-domain. Because of this, the present approach constrains the nodes to "slide" on the original inter-domain boundary, using the static equilibrium equation to keep the nodes proportional. The same method is used on a symmetry boundary, and the inflow boundaries nodes are not allowed to move. Constraining some of the nodes also speeds up the matrix inversion process, and allows a linear decrease of computation time proportional to the number of processors.

CFL condition

Since a new flux is introduced into the equations, the CFL condition needs to be adjusted accordingly. In the context of an implicitly coupled ablation-flow code, the recession distance is imposed: the node velocity is therefore a function of the time step. This translates to

$$\Delta t = \frac{l}{\sqrt{(u_n - \bar{w}_n)^2 + u_t^2 + u_p^2} + a}$$

This equation can be solved for Δt, and yields

$$\Delta t = \frac{l^2 - l_s^2}{(la - l_s u_n) + \sqrt{(la - l_s u_n)^2 - (l^2 - l_s^2)(a^2 - |u|^2)}}$$

where l is the characteristic length of the cell, $l_s = \frac{\Delta V}{S}$ the characteristic length of the volume increment of the face, and a is the speed of sound.

IV.C. Strong coupling implementation

Because re-entry simulations are being performed by computing steady-state solutions at multiple points of a discretized trajectory, the thermal response code is directly integrated as a boundary condition subroutine of LeMANS, thus taking advantage of the implicit nature of the code as well as the aggressive CFL ramping. The method used is similar to the one described in Ref. 2, and is illustrated in Fig. 1. Since MOPAR is 1-D, normal solution lines within the wall are traced at each boundary cell, and are computed sequentially. Because there is no need to compute the material response at every flow field iteration, MOPAR is called at a pre-determined number of iterations. This coupling method was previously presented,[5] but without having the fluid mesh being adapted. Even though the method showed good results and proved to be efficient and robust, the material response was not accurate since the shock wave was calculated from the initial state of the geometry, without taking into account the recession of the wall.

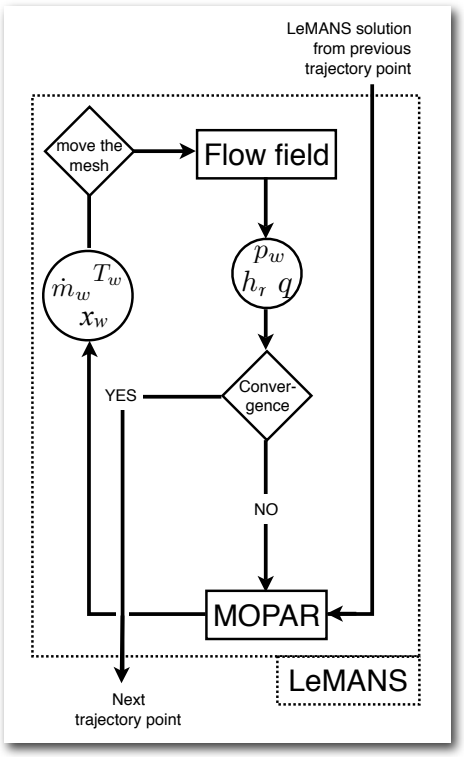

Figure 1. Coupling procedure for the integration of MOPAR in LeMANS

Three modifications are applied at the interface between the two codes to preserve stability and accelerate convergence. First, the convective heat flux used in MOPAR is adjusted using a hot-wall correction:[24]

$$q_{hw} = q_{cw}\Omega_{hw} = q_{cw}\left[\frac{\rho(T_{hw}, p_w)\mu(T_{hw})}{\rho(T_{cw}, p_w)\mu(T_{cw})}\right]^{0.1}$$

This method uses a boundary layer approximation to guess what the actual heat flux is supposed to be, and disappears once the wall has reached its converged values (i.e. when $T_{cw} = T_{hw}$, then $q_{cw} = q_{hw}$). The use of this correction speeds up the convergence of the wall temperature and ablation rates, and prevents the wall conditions from affecting the convergence of the flow field.

The second modification consists of damping the updated values at the wall. Instead of using the actual computed value given by the material response for recession distance, wall temperature and blowing rates, the value is combined with the one computed at the previous iteration:

$$T_{\text{assigned}} = (1 - \psi)T_{\text{old}} + \psi T_{\text{computed}}$$

The ψ parameter, usually set between 0.01 and 0.75, prevents the solution from being "caught" in an oscillation between two values, and also prevents the values from being over-evaluated (or under) while the solution is still changing.

A third modification is made to the moving boundaries condition by not imposing the mesh velocity at the wall. This way, while converging, the wall does not generate unphysical shock waves each time the mesh is moved back and forth.

Finally, the method used to couple the recession distance must be discussed. Because MOPAR is employed in each cell neighboring the wall, the recession distance is therefore calculated at the face of the cell. However, the moving mesh scheme presented here uses node velocities to move the wall (and the rest of the cells). Therefore, the face recession distance must be transformed into node velocities. In order to do so, the displacement of each node is taken as an average of each of its neighboring faces, and then divided by the time step to obtain a velocity. It is assumed that the mesh is sufficiently dense on the wall that this averaging method is accurate, therefore preserving the shape of the wall.

V. IRV-2 test case

In order to validate the strong coupling between MOPAR and LeMANS, the well documented[2,20] re-entry simulation of an IRV-2 vehicle is performed. This test case provides good feedback since it can be compared to other CFD-material response code coupling schemes, as well as to the ASCC code which uses flight data to generate results. The freestream conditions used in the discretized trajectory are presented in Table 1, and the material properties are set to generic non-charring carbon, using the properties given by Ref. 16. The ablation rates are interpolated from thermochemical tables generated by ACE-SNL[25] for carbon in air. Re-radiation is also included at the boundary. The mesh used for the simulation is presented in Fig. 2; it is important to point out that the material response calculations are carried out in one dimension, as described earlier. The triangular mesh presented in the figure is generated for post-processing analysis.

First, the results (without the moving mesh) for the temperature at the stagnation point for the whole re-entry trajectory are shown in Fig. 3. The results are in the same range as those published in the literature; the discrepancies are likely due to a difference in the physical properties used for the flow and wall chemistry, as well as a different TPS material: these parameters are not explicitly discussed in the references. It is to be noted that the overestimation in temperature in the first part of the trajectory, as well as the smoothness of the curve, is due to the fact that the whole material response surface history is plotted, as opposed to only the value at the discretized trajectory points. For this particular example, the coupled algorithm proved to be fast and robust for all the trajectory points (the results were obtained in roughly 18 hours, using 32 processors).

Table 1. Freestream conditions for the re-entry trajectory of the IRV-2 vehicle (from Ref. 2)

Trajectory point	Time [s]	Altitude [m]	Velocity [m/s]	Temperature [K]	Density [kg/m^3]
1	0.00	66935	6780.6	227.81	1.2505×10^{-4}
2	4.25	55842	6788.3	258.02	5.0454×10^{-4}
3	6.75	49290	6785.2	270.65	1.1344×10^{-3}
4	8.75	44042	6773.0	261.40	2.2593×10^{-3}
5	10.25	40108	6752.4	250.35	3.9957×10^{-3}
6	11.50	36836	6722.0	241.50	6.4268×10^{-3}
7	12.50	34229	6684.3	234.30	9.5832×10^{-3}
8	13.25	32283	6644.9	228.76	1.3145×10^{-2}
9	13.95	30480	6596.7	226.91	1.7313×10^{-2}
10	14.75	28236	6527.1	224.73	2.4310×10^{-2}
11	15.50	25772	6428.3	222.35	3.5348×10^{-2}
12	16.25	22949	6286.6	219.47	5.5888×10^{-2}
13	17.00	19790	6091.7	216.65	9.1741×10^{-2}
14	17.75	16355	5836.4	216.65	1.5635×10^{-1}
15	18.25	13962	5631.8	216.65	2.2786×10^{-1}
16	18.50	12748	5519.6	216.65	2.7946×10^{-1}
17	18.75	11528	5401.2	216.65	3.3743×10^{-1}
18	19.00	10309	5277.1	221.31	3.9840×10^{-1}
19	19.50	7892	5014.3	236.86	5.3196×10^{-1}
20	20.00	5536	4736.5	252.11	6.9366×10^{-1}
21	20.50	3273	4449.6	267.04	8.8610×10^{-1}
22	21.00	1129	4159.7	280.68	1.0954×10^{-0}
23	21.28	0	4000.0	288.15	1.2250×10^{-0}

Figures 4 and 5 illustrate the results obtained using the moving mesh algorithm presented here. As can be seen for, the surface remains smooth even though the coupling is aggressive, as the vehicle ablates toward its final shape. It is also important to note that even though the mesh is relatively rough at the wall, especially in the tangential direction, the face-to-node interpolation remains very accurate. It is also

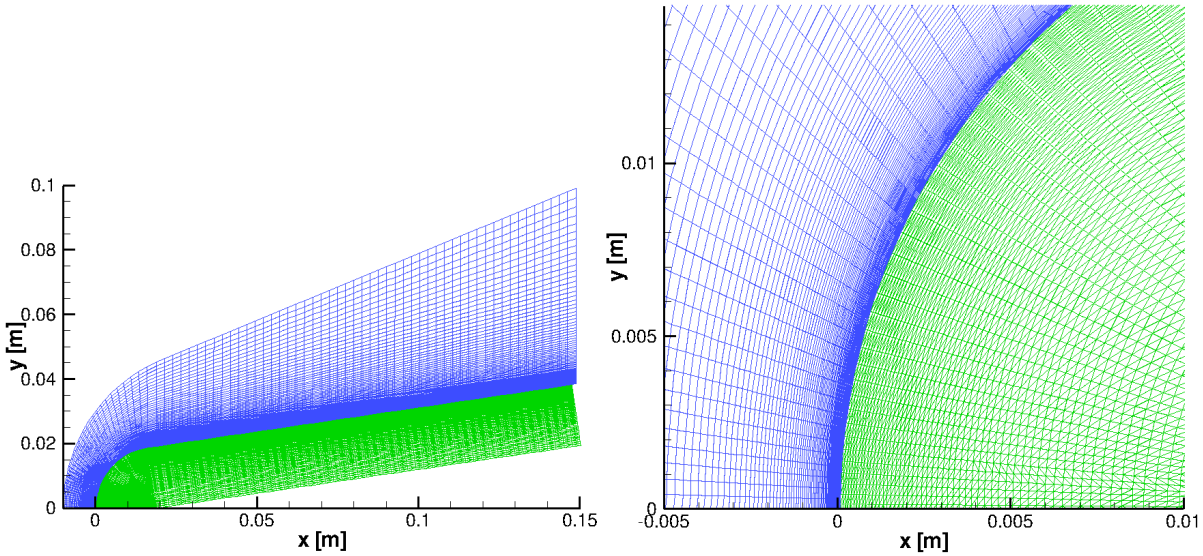

(a) Overall view of the meshes

(b) Close up view of the meshes

Figure 2. Flow field mesh and material response mesh used for the simulation of the re-entry of the IRV-2 vehicle, at trajectory point 2 of Table 1

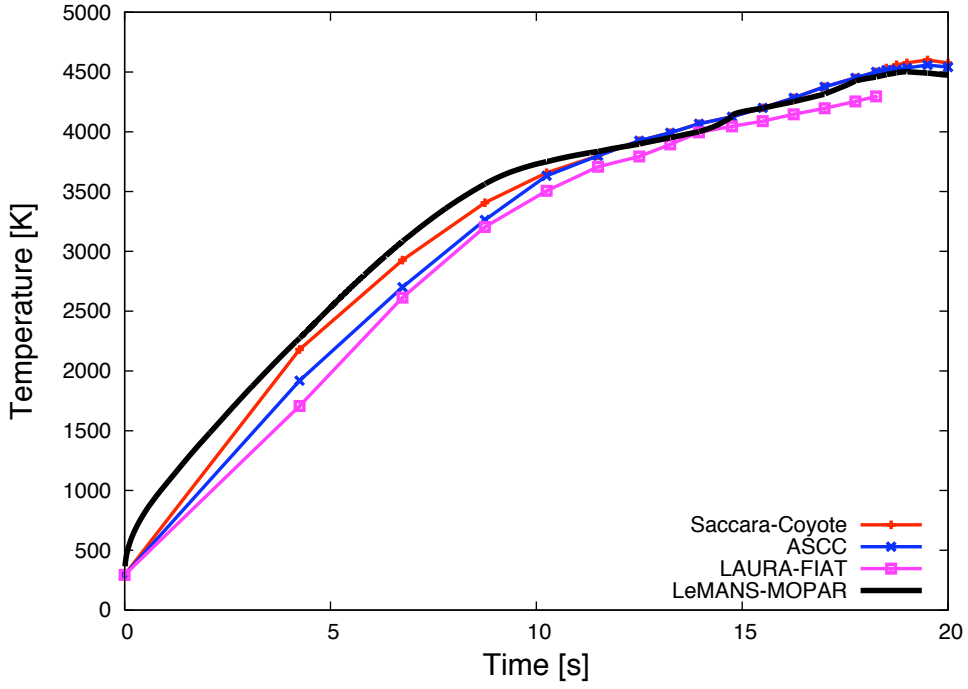

Figure 3. Temperature at the stagnation point of the IRV-2 re-entry vehicle at the trajectory points of Table 1: comparison with numerical results of Ref. 2 and Ref. 20

important to remember that the calculations presented in these figures are performed using non-equilibrium thermodynamics and that only the translational temperature is plotted. As some of the energy is increasingly transfered to the vibrational modes, the translational temperature decreases, but not necessarily the total energy as one might be led to believe.

Next, in Figs. 6, the recession distance and surface temperature are compared to results obtained with the ASCC code, which includes flight data, and with the coupled Coyote-Saccara codes,[2] for the first half of the trajectory. As can be seen, the results are within the expected range, especially given that thermodynamic values and ablation rates for a generic carbon-carbon ablator are used (the ablator properties are not reported for the compared results).

Figure 7 shows the surface properties during the first half of the trajectory. As can be seen, the solution deteriorates over time; this is especially true for sensitive quantities such as heat flux and blowing rates. This is explained by the fact that the slight imprecision in one solution is ported and amplified at each subsequent trajectory point. This loss of precision is attributed in part to the fact that the method used for mesh movement is influenced by the flow field solution, since the inter-processor boundaries are not allow to be displaced. Thus, the perpendicularity to the surface is affected as the surface recesses, therefore deteriorating the solution on the adjacent cells. The coarseness of the mesh might also have an impact on the loss of precision. As an additional error source, the lack of a mesh quality verification algorithm causes the mesh to become misaligned with the shock, which usually results in errors in the heat flux at the surface.

Finally, it is important to note that the results for temperature and recession rates remain smooth and clean throughout the trajectory. Because these two parameters are very important to heat shield design, the results are very encouraging.

VI. Conclusion

To improve heat and ablation rate modeling on hypersonic re-entry vehicles, a material response model has been strongly coupled to an hypersonic flow solver. To demonstrate the coupling between the flow solver LeMANS and the material response code MOPAR, a simulation of the re-entry trajectory of an IRV-2 vehicle is presented. The numerical results are within the expected range, especially considering the many unknown parameters, and the coupling method used shows stability, robustness and efficiency during the simulation. However, from these results, it is clear that to improve the solutions and prevent repercussion of imprecision towards later trajectory points, a mesh quality verification algorithm must be included.

References

[1]Ahn, H.-K., Park, C., and Sawada, K., "Dynamics of Pyrolysis Gas in Charring Materials Ablation," *AIAA 36th Aeros. Sci. Meeting*, No. AIAA-1998-0165, January 1998, p. 11.

[2]Kuntz, D., Hassan, B., and Potter, D., "Predictions of Ablating Hypersonic Vehicles Using an Iterative Coupled Fluid/Thermal Approach," *Journal of Thermophysics and Heat Transfer*, Vol. 15, No. 2, 2001, pp. 129–139. doi:10.2514/2.6594

[3]Gnoffo, P. A., Johnston, C. O., and Thompson, R. A., "Implementation of Radiation, Ablation, and Free Energy Minimization Modules for Coupled Simulations of Hypersonic Flow," *47th AIAA Aerospace Sciences Meeting and Exhibit*, No. AIAA 2009-1399, Orlando, FL, January 5-8 2009, p. 12.

[4]Nompelis, I., Candler, G., and Conti, R., "A Parallel Implicit CFD Code for the Simulation of Ablating Re-Entry Vehicles," *47th AIAA Aerospace Sciences Meeting and Exhibit*, No. AIAA-2009-1562, Jan. 5-8 2009.

[5]Martin, A. and Boyd, I. D., "Simulation of pyrolysis gas within a thermal protection system," *40th AIAA Thermophysics Conference*, No. AIAA-2008-3805, Seattle, WA, June 23-26 2008, p. 20.

[6]Martin, A. and Boyd, I. D., "Implicit implementation of material response and moving meshes for hypersonic re-entry ablation," *47th AIAA Aerospace Sciences Meeting and Exhibit*, No. AIAA-2009-0670, Orlando, FL, Jan. 5-8 2009.

[7]Scalabrin, L. C. and Boyd, I. D., "Numerical Simulations of the FIRE-II Convective and Radiative Heating Rates," *39th AIAA Thermophysics Conference*, No. AIAA-2007-4044, Miami, FL, 25 - 28 June 2007, p. 17.

[8]Scalabrin, L. C., *Numerical Simulation of Weakly Ionized Hypersonic Flow Over Reentry Capsules.*, Ph.D. thesis, The University of Michigan, Ann Arbor, MI, 2007.

[9]Scalabrin, L. C. and Boyd, I. D., "Development of an Unstructured Navier-Stokes Solver for Hypersonic Nonequilibrium Aerothermodynamics," *38th AIAA Thermophysics Conference*, No. AIAA-2005-5203, Toronto, Ontario, June 6-9 2005, pp. 1–18.

[10]Scalabrin, L. C. and Boyd, I. D., "Numerical Simulation of Weakly Ionized Hypersonic Flow for Reentry Configurations," *9th AIAA/ASME Joint Thermophysics and Heat Transfer Conference*, No. AIAA-2006-3773, San Francisco, CA, June 5-8 2006, p. 18.

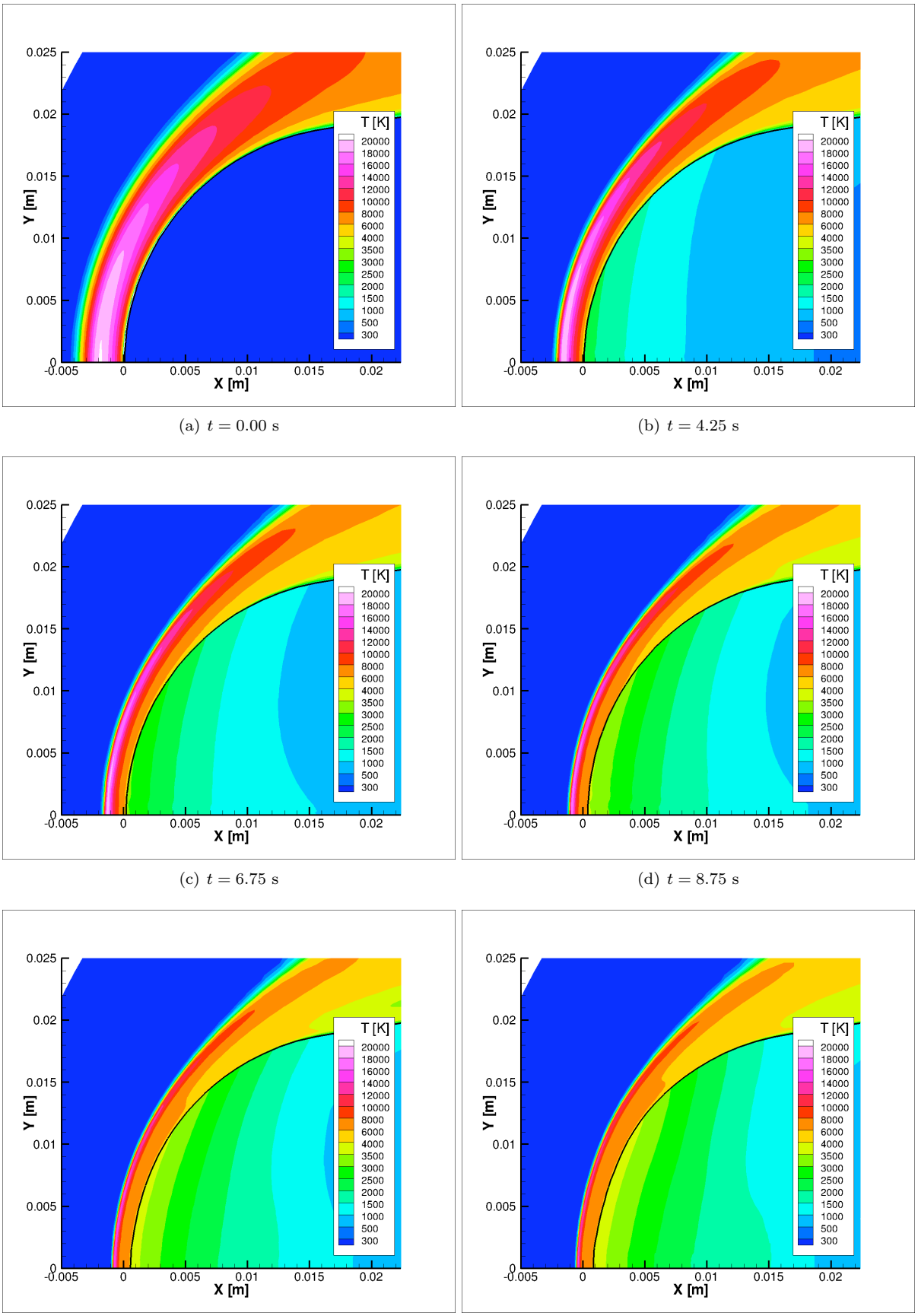

(a) $t = 0.00$ s

(b) $t = 4.25$ s

(c) $t = 6.75$ s

(d) $t = 8.75$ s

(e) $t = 10.25$ s

(f) $t = 11.50$ s

Figure 4. Translational temperature of the flow field and temperature in the solid wall of the IRV-2 re-entry vehicle at trajectory points 1 through 6 of Table 1

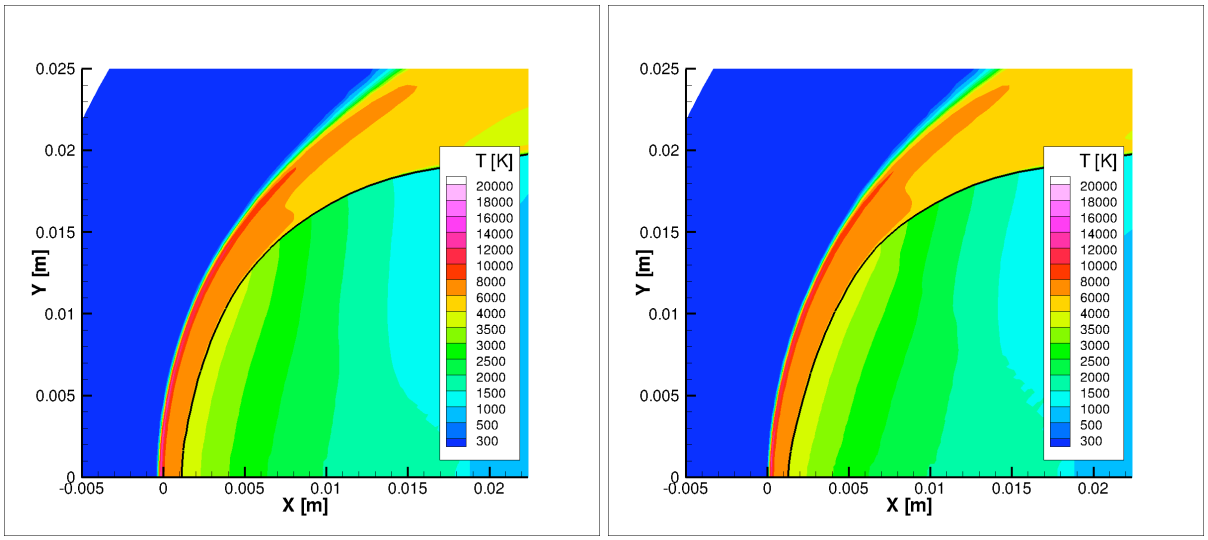

(a) $t = 12.50$ s

(b) $t = 13.25$ s

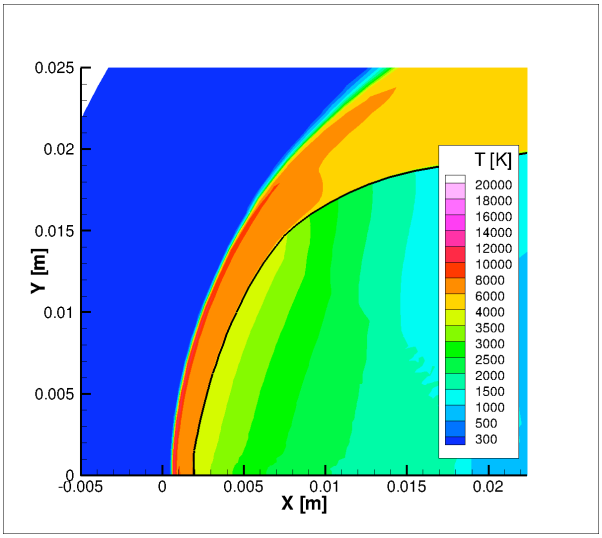

(c) $t = 13.95$ s

Figure 5. Translational temperature of the flow field and temperature in the solid wall of the IRV-2 re-entry vehicle at trajectory points 7 through 8 of Table 1

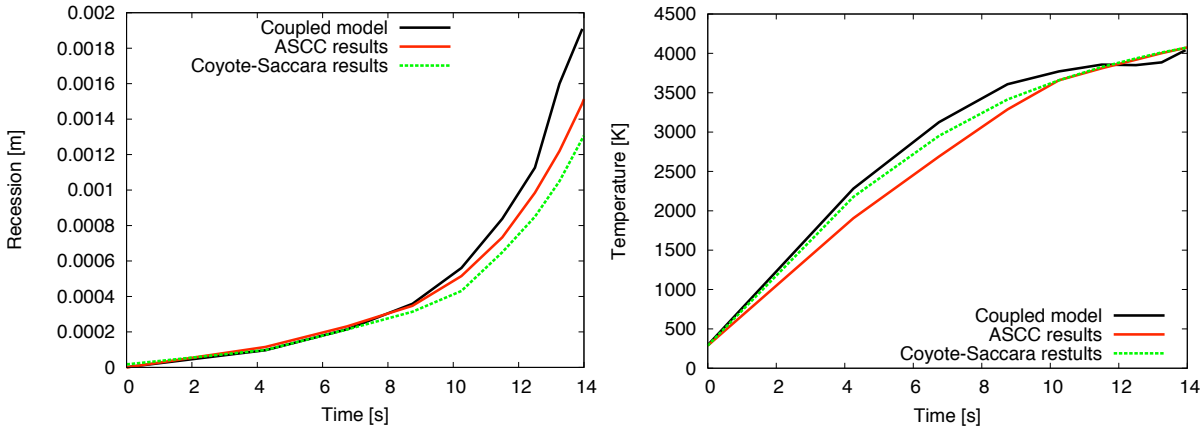

(a) Surface recession (b) Surface temperature

Figure 6. Comparison of surface recession and surface temperature at the stagnation point during re-entry for the IRV-2 vehicle

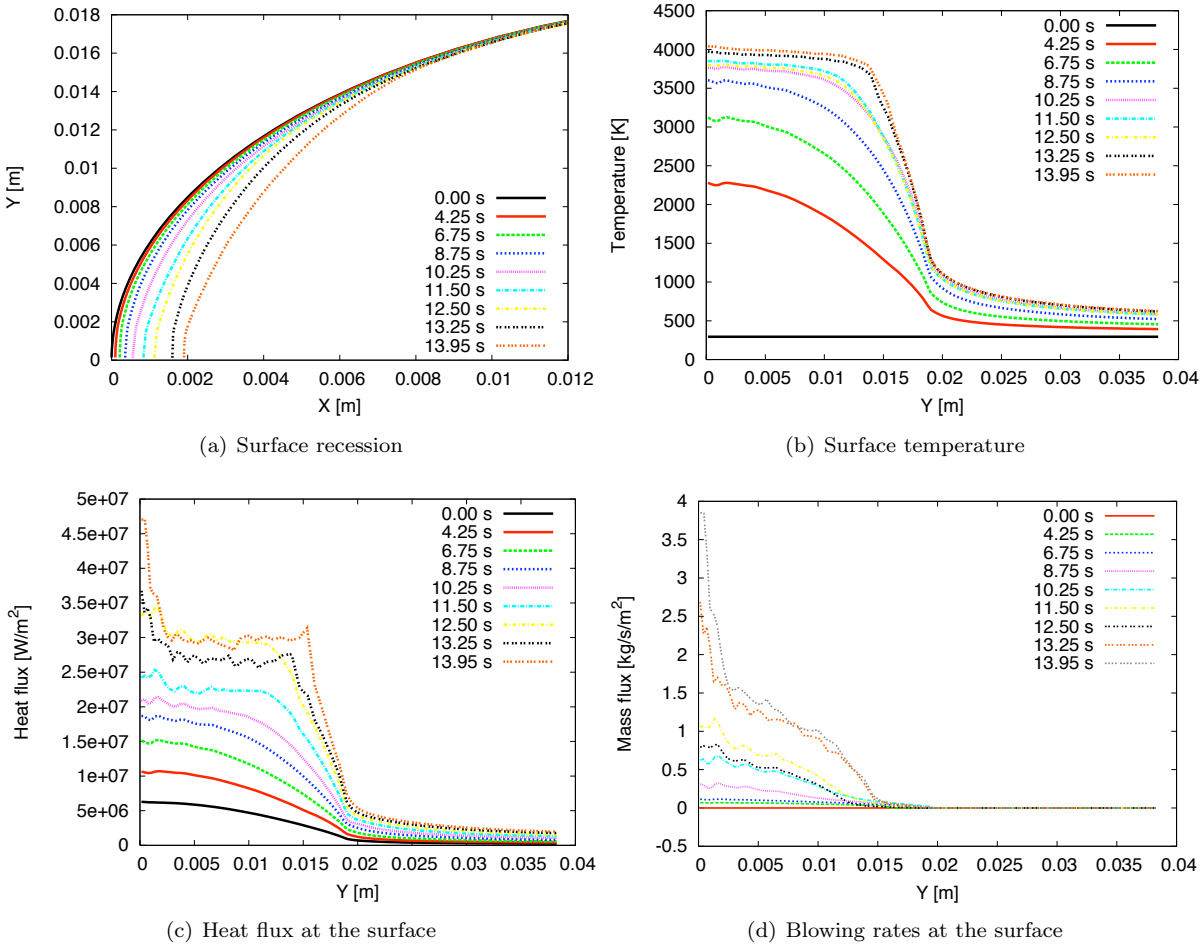

(a) Surface recession (b) Surface temperature

(c) Heat flux at the surface (d) Blowing rates at the surface

Figure 7. Surface properties during re-entry for the IRV-2 vehicle

[11]Holman, J. P., *Heat transfer*, Mc Graw-Hill : Publishing Company, 1990.

[12]Wright, M. J., Candler, G. V., and Bose, D., "Data-Parallel Line Relaxation method for the Navier-Stokes equations," *AIAA Journal*, Vol. 36, No. 9, September 1998, pp. 1603–1609.
doi:10.2514/2.586

[13]Gnoffo, P. A., "Upwind-Biased, Point-implicit Relaxation Strategies for Viscous Hypersonic Flows," *9th AIAA Computational Fluid Dynamics Conference*, No. AIAA-1989-1972-CP, Buffalo, NY, June 13-15 1989, pp. 415–425.

[14]Martin, A. and Boyd, I. D., "Non-Darcian behavior of pyrolysis gas in a thermal protection system," *Journal of Thermophysics and Heat Transfer*, 2009.
doi:10.2514/1.44103

[15]Blackwell, B. F. and Hogan, R. E., "One-Dimensional Ablation Using Landau Transformation and Finite Control Volume Procedure," *Journal of Thermophysics and Heat Transfer*, Vol. 8, No. 2, April-June 1994, pp. 282–287.
doi:10.2514/3.535

[16]Amar, A. J., *Modeling of One-Dimensional Ablation with porous Flow Using Finite Control Volume Procedure*, Master's thesis, North Carolina State University, Raleigh, NC, 2006.

[17]Amar, A. J., Blackwell, B. F., and Edwards, J. R., "One-Dimensional Ablation Using a Full Newton's Method and Finite Control Volume Procedure," *Journal of Thermophysics and Heat Transfer*, Vol. 22, No. 1, January 2008, pp. 72–82.
doi:10.2514/1.29610

[18]Amar, A. J., Blackwell, B. F., and Edwards, J. R., "Development and Verification of a One-Dimensional Ablation Code Including Pyrolysis Gas Flow," *Journal of Thermophysics and Heat Transfer*, Vol. 23, No. 1, January–March 2009, pp. 59–71.
doi:10.2514/1.36882

[19]Martin, A. and Boyd, I. D., "Variation of the Thomas algorithm for opposed-border tridiagonal systems of linear equations," *Communications in Numerical Methods in Engineering*, 2008.
doi:10.1002/cnm.1172

[20]Thompson, R. A. and Gnoffo, P. A., "Implementation of a Blowing Boundary Condition in the LAURA Code," *46th AIAA Aerospace Sciences Meeting and Exhibit*, No. AIAA-2008-1243, Reno, NV, Jan. 7-10 2008, p. 11.

[21]Martinelli, S. and Ruffin, S., "Validation Process for Blowing and Transpiration-Cooling in DPLR," *39th AIAA Thermophysics Conference*, No. AIAA-2007-4255, 2007, p. 9.

[22]Zhang, H., Reggio, M., Trépanier, J.-Y., and Camarero, R., "Discrete form of the GCL for moving meshes and its implementation in CFD schemes," *Computers & Fluids*, Vol. 22, No. 1, 1993, pp. 9–23.
doi:10.1016/0045-7930(93)90003-R

[23]Batina, J. T., "Unsteady Euler Airfoil Solutions Using Unstructured Dynamic Meshes," *27th Aerospace Sciences Meeting*, No. AIAA 89-0115, Reno, NV, January 9-12 1989.

[24]Cohen, C. B. and Reshotko, E., "Similar Solutions for the Compressible Laminar Boundary Layer with Heat Transfer and Pressure Gradient," Technical Note 3325, NACA, 1955.

[25]Powars, C. A. and Kendall, R. M., *Aerotherm Chemical Equilibrium (ACE) Computer Program - User's Manual*, Aerotherm Corporation, Mountain View, CA, May 1969.